Letter

Understanding native defect induced photoluminescence in Zn_2SnO_4

Ngoc Linh Nguyen,[1,2,*] Hung The Dang,[1,3] Manh Trung Tran,[1] Nguyen Van Du,[4] Nguyen Tu,[4] Do Quang Trung,[4] Le Thi Thao Vien,[5] and Pham Thanh Huy[1]

[1]*Faculty of Materials Science and Engineering, Phenikaa University, Hanoi 12116, Vietnam*
[2]*PHENIKAA Research and Technology Institute (PRATI), A&A Green Phoenix Group JSC, No. 167 Hoang Ngan, Trung Hoa, Cau Giay, Hanoi 11313, Vietnam*
[3]*Phenikaa Institute of Advanced Study (PIAS), Phenikaa University, Hanoi 12116, Vietnam*
[4]*Faculty of Fundamental Sciences, Phenikaa University, Hanoi 12116, Vietnam*
[5]*Natural Science Department, QuyNhon University, 170 An Duong Vuong, Quy Nhon, Binh Dinh 590000, Vietnam*

(Received 17 October 2022; revised 22 January 2023; accepted 31 January 2023; published 16 February 2023)

Simulation of photoluminescence spectroscopy from first principles provides a powerful approach for predicting the experimental spectrum and understanding the origin of the luminescence of materials. We show here that the use of the hybrid-exchange correlation functional combined with first-principles molecular dynamics can simulate the defect-induced photoluminescence spectrum of zinc stannate (Zn_2SnO_4) in good agreement with the experiment. The calculations were carried out for 12 different point defects of Zn_2SnO_4, and show that the green-to-red photoluminescence emissions obtained in the experiment are mainly contributed by the oxygen vacancy defects. These defect states play the roles of deep donors and radiative recombination centers during the photoluminescence mechanism. In particular, their electronic properties are significantly affected by temperature, which is related to the strong fluctuation of the nearest-neighbor Sn atoms relative to the vacancy center.

DOI: 10.1103/PhysRevB.107.L060102

Over the past two decades, zinc stannate (Zn_2SnO_4), a transparent semiconducting oxide, has attracted much attention from researchers thanks to its wide range of applications, including humidity and gas sensors [1], transparent conductors [2,3], anodes for lithium-ion batteries [4–6], electrodes for dye-sensitized solar cells [7,8], and photocatalysis [9], to name a few. In particular, its wide band gap (≈3.7 eV) [10] allows for native defects or impurity doping into the system at various energy levels inside the band gap, resulting in light emissions of a wide range of colors from this material. A few examples that have been reported so far are blue [11–13], green [9,12,13], yellow-orange [9,13,14], and red [15,16] colors. In particular, recently, Vien *et al.* [16] have shown that single-phase Zn_2SnO_4 powder synthesized from ZnO and SnO_2 can have a very bright emission at wavelength 684 nm even at room temperature as observed in the photoluminescence (PL) spectrum. This emission is in the middle of the far-red color regime (670–730 nm), which is highly important for designing high luminous efficacy and high color rendering index white light-emitting diode (LED) devices [17]. Hence, Zn_2SnO_4 can be a potential candidate to coat LED chips for white LED devices or even for agricultural applications where light-based stimulating plant growth requires red or far-red light emissions [18].

However, at the current stage, the physics for the PL spectrum of Zn_2SnO_4 are not fully understood. As mentioned previously, because of the wide band gap, the PL spectrum of Zn_2SnO_4 is defect mediated where the transition energies smaller than the band gap are in focus. But except for the rather obvious band-to-band emission peak near the band-gap value 3.7 eV [19,20], the contributions of defects to Zn_2SnO_4 optical properties are still ambiguous and under controversy [9,20]. Almost all possible types of native defects with finite thermodynamic stability and lattice distortion defects have been considered as potential emission centers for Zn_2SnO_4 to understand its luminescence spectrum. For example, blue and green emissions may be attributed to oxygen vacancies and lattice distortions may result in [9,11,12,19,21,22] orange and red emission bands attributed to not only oxygen vacancies but also Sn and Zn interstitials [15,23,24]. Furthermore, the synthesis condition is an important factor that controls the chemical potentials of each Zn, Sn, or oxygen element, lattice structure, defect concentrations, etc. [9], causing difficulties in establishing a correct relationship between defect structures and the luminescence spectrum of Zn_2SnO_4. So far, the consensus is that oxygen vacancy is the main reason for the blue and green emission bands [19,22], and the origins of other emission bands are not clearly explained. Moreover, these are mostly explanations based on experimental evidence, and a fully theoretical interpretation of the PL spectrum is missing. Therefore, having an accurate theoretical framework to interpret the experimental luminescence results and make predictions of other emission bands for Zn_2SnO_4 samples is essential.

There are very few theoretical works studying defect states in Zn_2SnO_4, mostly focusing on the oxygen vacancies [25] and lacking information on their luminescence properties. In

*linh.nguyenngoc@phenikaa-uni.edu.vn

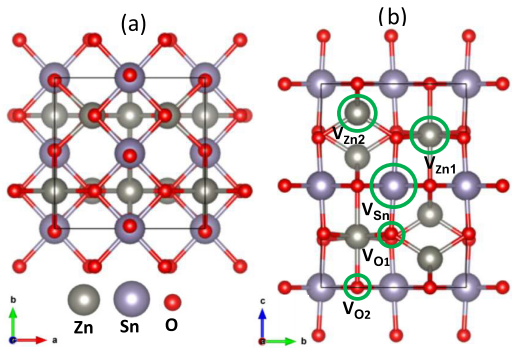

FIG. 1. Top (a) and side (b) views of the ball-and-stick model of the Zn_2SnO_4 crystal unit cell. The structures have single oxygen, Zn, or Sn vacancy and their names are defined by removing the corresponding atom marked by the blue circles. Here, V_{O1} and V_{O2} are formed by removing oxygen atoms at the sites surrounded by (3 Zn and 1 Sn) and (2 Zn and 2 Sn) atoms, respectively. V_{Zn1} and V_{Zn2} are formed by removing Zn atoms from the octahedrally and tetrahedrally coordinated sites, respectively. V_{Sn} structure is unique because all the Sn atoms in the system are symmetrically equivalent. a, b, and c indicate the directions of the three primitive lattice translation vectors of the system, of which the computed lengths are presented in Table I.

this Letter, by using extensive first-principle simulations, we aim to study systematically the electronic properties and the PL spectrum for each type of defect in Zn_2SnO_4. This result provides a detailed interpretation of the origin of the near-, far-red, and green-emission peaks in the PL spectrum of Zn_2SnO_4 which has been summarized in Ref. [20]. In particular, using our first-principles approach, we present the calculated PL spectra of this system consistent with experimental results, providing a reliable method to study the PL spectra of materials.

Experiments have shown that the ternary oxide Zn_2SnO_4 has an inverse spinel stable phase [10,26–28], where one Zn atom in the chemical formula is tetrahedrally coordinated while the other Zn atom and the Sn atom are octahedrally coordinated in equal proportion. This phase is shown to exist as a single phase by heating the composition of ZnO and SnO_2 to $T = 1275\,^{\circ}$C and then annealing to room temperature [29,30]. However, it is not clear from the research community about the exact symmetry of the crystal structure, especially about the cation ordering. Reference [31] examined various possible crystal symmetries of Zn_2SnO_4 using first-principles calculations, suggesting that the correct symmetry depends much on the pressure and temperature of the system. If the cation is disordered, Zn_2SnO_4 is likely to be in a cubic space group ($Fd\bar{3}m$) [32]. In contrast, at a certain pressure and temperature where the cation ordering might exist, then the higher chance is that the more favorable space groups are orthorhombic structures *Imma* or $P4_122$ [31–35]. Furthermore, Bao *et al.* [33] showed strong evidence that *Imma* symmetry can be stabilized for Zn_2SnO_4. Therefore, in our Letter, we relax the system using the initial *Imma* crystal structure. In this orthorhombic symmetry group, Zn_2SnO_4 exhibits an inverse spinel crystal structure (see Fig. 1) where the unit cell has 28 atoms (consisting of 8 Zn, 4 Sn, and 16 oxygen atoms). Starting with the *Imma* structure obtained from the

TABLE I. The lattice parameters (a, b, c) of the orthogonal Zn_2SnO_4 unit cell and the atomic bond lengths of Zn–O and Sn–O bonds (in Å) computed using PBE and PBE0 functionals and compared with experiments.

	PBE	PBE0	Expt.
a	6.09	6.11	6.09 [35]
b	6.31	6.12	6.09 [35]
c	8.78	8.59	8.62 [24], 8.50 [35]
Sn–O	2.06	2.05	
Zn–O	2.07	2.06	

Materials Project database [36], we employ the first-principles variable-cell relaxation method [37] to obtain the most stable crystal structure. The optimized lattice parameters and atomic bond lengths are shown in Table I.

Defect in Zn_2SnO_4 is simulated by constructing a supercell of $3 \times 3 \times 2$ pristine orthogonal Zn_2SnO_4 cells, containing 504 atoms in total, and then a single defect is imposed in the supercell. We consider all possible 12 point defects that may occur in Zn_2SnO_4, which are divided into three types: vacancies, interstitial defects, and antisites. Vacancy defects are constructed by removing the oxygen, Sn, or Zn atom at symmetrically inequivalent sites, forming five different defects, namely, V_{O1}, V_{O2}, V_{Zn1}, V_{Zn2}, and V_{Sn} (see Fig. 1). Interstitial defects are formed by inserting the oxygen, Sn, or Zn atom into the center of the biggest unoccupied region of the cell, resulting in three defects Zn_i, Sn_i, and O_i. Finally, by replacing one atom in the cell with a different atom denoted as A_B (atom B replaced by atom A), one obtains four kinds of antisite defects: Zn_{Sn}, Zn_O, Sn_O, and Sn_{Zn}. Density functional theory (DFT) is employed with the plane-wave and pseudopotential methods developed in the QUANTUM ESPRESSO package [38,39] for our calculations. The structures with defects are optimized at 0 K by using the Broyden-Fletcher-Goldfarb-Shanno algorithm [40]. The SG15 optimized norm-conserving Vanderbilt pseudopotentials [41] are used for the electron-ion interactions. The energy cutoff for the plane wave expansion is 100 Ry (400 Ry for the charge density cutoff). Brillouin-zone integration has been performed using single-Γ point sampling and a $6 \times 6 \times 6$ k grid for the Zn_2SnO_4 supercell and pristine unit cell, respectively. Detailed atomic coordinates of all optimized structures are presented in the Supplemental Material (SM) [42].

We calculate PL spectra theoretically following Fermi's "golden rule" [43], which describes radiative recombination between an excited electron lying at the conduction band minimum (CBM) φ_{CBM} and a hole residing at the deep defect state, φ_d, of which the energy level is in the band gap of the semiconductor:

$$PL(\omega) = \sum_d \mathcal{N}\omega^2 |\langle \varphi_{\mathrm{CBM}} | \hat{r} | \varphi_{\mathrm{d}} \rangle|^2 \times \delta(\epsilon_{\mathrm{CBM}} - \epsilon_{\mathrm{d}} - \omega). \quad (1)$$

Here, $\hat{r}$ is the position operator, and ϵ_{CBM} and ϵ_{d} are the energy levels at the CBM and defect state, respectively. $\mathcal{N}$ stands for the normalization factor. In our calculations, the main recombination mechanism leading to PL emissions is the band-to-defect transition [43,44] while other possible mechanisms such as band-to-band, excitonic, or defect-to-defect

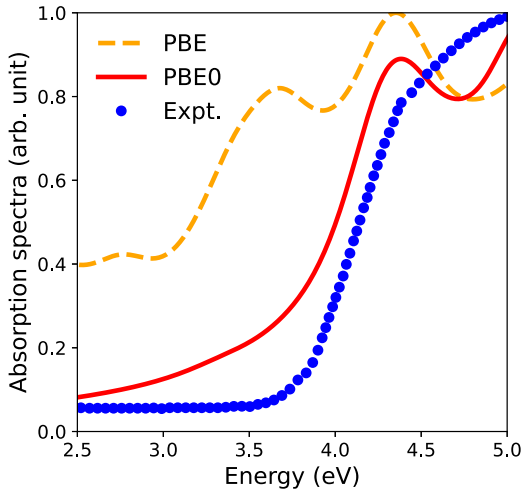

FIG. 2. Total theoretical and experimental optical absorption spectra for the pristine Zn_2SnO_4 crystal. The theoretical spectra are calculated with PBE and PBE0 functionals, which are averaged over the x, y, and z directions. The experimental spectrum is taken from Ref. [20]

transition are not considered, mostly because their transitional energy is out of the PL energy window of interest. The single-particle states φ's and the energy levels ϵ's in Eq. (1) are obtained from the solutions of the Kohn-Sham equation in the DFT calculations. We note that the complete formula for the PL spectra [43] contains the electron (hole) occupancy in the initial (final) state. However, as there are only deep defect states, the excited electrons stay mostly around the CBM while the hole occupancy at the defect states is always unity, justifying Eq. (1).

We start with a discussion of an appropriate exchange-correlation functional used in DFT calculations for predicting structural properties, electronic band gap E_g, and optical spectroscopy of Zn_2SnO_4. Two approximation levels, the Perdew-Burke-Ernzerhof (PBE) generalized gradient approximation functional [45] and the PBE0 hybrid functional [46], are considered for calculations of Zn_2SnO_4 using a pristine unit cell. Both functionals predict a direct band gap for this material. However, while the PBE0 functional predicts an E_g value of 3.35 eV, compatible with experimentally reported values ranging from 3.3 to 3.7 eV [9,26,47], the PBE functional reports $E_g \approx 1.3$ eV, severely underestimating it. This failure of PBE for predicting the band gap is due to its self-interaction error [48] and the lack of piecewise linearity behavior of total energy as a function of occupation [49]. Moreover, thanks to its high macroscopic dielectric constant ($\epsilon_\infty \approx 10.23$), absorption spectra can be calculated within the random phase approximation [50] for Zn_2SnO_4. The results are plotted in Fig. 2, showing that the PBE0 functional predicts well the absorption spectrum of the system, not only the onset of the absorption peak but also the peak position in the range from 2.0 to 5.0 eV, while the PBE one is not consistent with the experimental one.

However, the discrepancy between the PBE0 and PBE functionals when predicting structural properties of the pristine Zn_2SnO_4 is less pronounced. Table I shows the average atomic bond lengths of Sn–O and Zn–O bonds and three lattice constants computed using PBE0 and PBE functionals in comparison with the experimental values. Lattice constants and bond lengths from PBE calculations are only less than 2 and 1% different from those from PBE0 ones, respectively. These calculated lattice constants are less than 3% different from the x-ray diffraction experimental data measured in Zn_2SnO_4 nanoparticles [24] and in one-dimensional Zn_2SnO_4 nanostructures stabilizing in an inverse spinel orthorhombic phase at high pressure [35], confirming the reliability of both PBE and PBE0 functionals in predicting the lattice structure. Therefore, because of the computational expense of the PBE0 functional, our approach to simulate Zn_2SnO_4 with defects effectively is first to compute the optimized structure with the PBE functional, and then conduct rigorously electronic structure and PL spectrum calculations with the PBE0 functional.

Choosing a reliable exchange-correlation functional and having a lattice structure that matches the experiment allow us to analyze and discuss in detail the electronic structure of the defect states and their corresponding PL brightness by calculating the Zn_2SnO_4 structure with defects at 0 K. We find that all kinds of interstitial or antisite defects have a negligible contribution to the overall PL spectra (see the Supplemental Material [42]), therefore they are not considered in the main text. Then, we plot in Fig. 3 the spin-resolved energy-level diagram of the vacancy defects only (V_{O1}, V_{O2}, V_{Sn}, V_{Zn1}, and V_{Zn2}). The common point for all these types of vacancies is that the energy levels are inside the band gap, thus directly contributing to the PL spectra of Zn_2SnO_4. Figures 3(a) and 3(b) characterize the defect states of oxygen vacancies V_{O1} and V_{O2}, respectively. They are spin-non-polarized and fully occupied midgap states that hybridize more strongly with adjacent Sn atomic orbitals than with those of Zn, resulting in the defect energy level (Kohn-Sham level) of 1.95 eV (1.55 eV) above the valence band maximum (VBM) for V_{O1} (V_{O2}), and therefore acting as donors. These energy values are in the same order as the results reported in Ref. [25]. It is also worth mentioning that the formation energy of oxygen vacancy V_{O1} is higher than that of V_{O2}, suggesting that under the same synthesis condition V_{O2} may be easier to be formed than V_{O1}.

In contrast, as the Sn or Zn atom in the pristine structure is removed, their vacancies result in unoccupied defect states, thus acting as acceptors. Interestingly, these defect structures exhibit ferromagnetic order with the magnetization of $2\mu_B$ and $4\mu_B$, where μ_B is the Bohr magneton constant, for Zn and Sn vacancies, respectively [see Figs. 3(c), 3(d) and 3(e)]. The ferromagnetism induced by the Zn vacancy has also been reported in ZnO [51,52] where the magnetic moment is primarily delivered from the O-2p states, which coordinate with the Zn vacancy. They align via the p-p orbital coupling mediated by hole carriers at the defect, leading to ferromagnetism [51]. The same mechanism is likely to occur in Zn_2SnO_4 where the vacancies are located at the octahedral or tetragonal sites, similar to ZnO. According to our calculations, V_{Sn} has two twofold degenerate defect states at 1.0 and 2.45 eV above the VBM, whereas each type of Zn vacancy causes two defect energy levels for V_{Zn1} and V_{Zn2}, respectively (0.95 and 0.2 eV) and (1.15 and 1.05 eV). As exhibited in Fig. 3, the defect states of Sn and Zn vacancies are p^*-type orbitals, which are less localized than those of oxygen vacancies and allocated at oxygen sites adjacent to these vacancies.

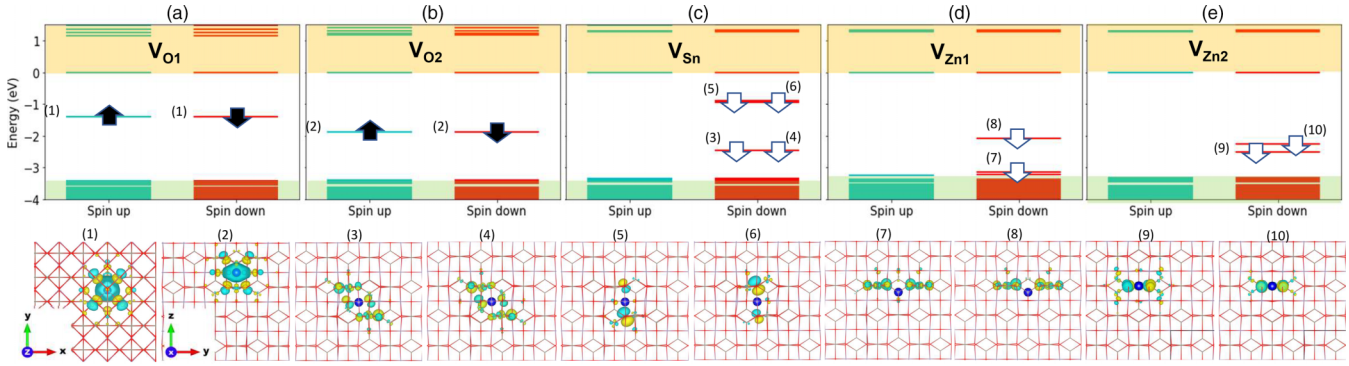

FIG. 3. Top panel: The electronic structures of the five Zn_2SnO_4 vacancy-defect models. The deep defect states are denoted with black or white arrows corresponding to occupied or unoccupied states, respectively. The up (down) arrow is corresponding to the spin channel up (down) of the Kohn-Sham states, respectively. Bottom panel: Visualization of the density isosurfaces with the isovalue of 4×10^{-4} (e/bohr^3) for the defect states numbered in the top-panel figures. The host Zn_2SnO_4 crystal is visualized in the wire-frame model. The blue balls denote the vacancy defect position. The two different colors of the density isosurfaces refer to the sign of the wave function. Here, to show symmetry of the defect orbitals, the supercell of the V_{O1} is projected along the [001] direction, while for the others it is projected along the [100] direction. The crystal coordinate axes of the system are denoted as (x, y, z).

Based on the electronic structures of Zn_2SnO_4 with defects, one can calculate the PL spectra of the material. This type of calculation is conducted in two steps: first, the PL spectrum for each type of defect structure is obtained by employing Eq. (1); second, the total PL spectrum is estimated by averaging over all defect-dependent PL spectra, which can be used to compare with experimental results. We further note that the experimental PL spectrum for reference is obtained from Ref. [20], in which the photon energy window is restricted to the range from 1.4 to 2.6 eV, hence we focus our calculations mostly in this energy range. In the first step, we examine PL spectra for each type of defect and discover that oxygen vacancies produce a bright peak at ≈1.4 eV (857 nm) and ≈1.8 eV (666 nm), respectively, for V_{O1} and V_{O2}, while other defects produce darker peaks within the visible energy window. Here, we note that V_{Sn} and Zn_O can generate emission peaks at ≈0.9 eV (1333 nm) and at ≈0.5 eV (2254 nm), respectively, whose PL intensity is in the same order as that of the oxygen vacancies (see Fig. 3 of the SM [42]). However, their energy is out of the energy window of interest, and they thus are not considered in the following. These behaviors reflect a trend that the low-energy optical transitions are more likely to occur than those of the high-energy ones.

In the second step, we compute the total PL spectrum at zero temperature by averaging PL spectra of all types of defects and compare them with the experimental data obtained from Ref. [20]. For this comparison, we align the highest peak of computational and experimental spectra and determine the relative positions of other peaks to this by applying a 0.2-eV blueshift and normalizing the highest peak of both the computational and experimental spectra to one. Figure 4 exhibits these spectra, showing the consistency between experiment and calculation, especially our first-principle calculations, which predict the correct relative position between the main and the second main peaks. The second main peak is in the green region (≈2.3 eV) caused by V_{O2}, which agrees with the oxygen-vacancy-related green emission reported in Ref. [19]. However, the portion of spectral weight from 1.9 eV (red emission) to 2.2 eV (green emission) is not depicted by the zero-temperature spectrum. Because contributions from antisites or interstitials are negligible, there are two main reasons for consideration. The first reason may come from further mechanisms of the optical transition that we do not consider in this Letter, such as the carrier lifetime or scattering process, which may broaden the PL peaks into the red-to-green region. However, the chance for this is low because the energy range of the discrepancy is too large for such a broadening. The higher chance is from the difference in temperature in use. Because the experimental spectrum is measured at room temperature (300 K), thermal relaxation effects must be taken into account.

To test this claim, we perform first-principle molecular dynamics (MD) simulations on Zn_2SnO_4 with defects at 300 K,

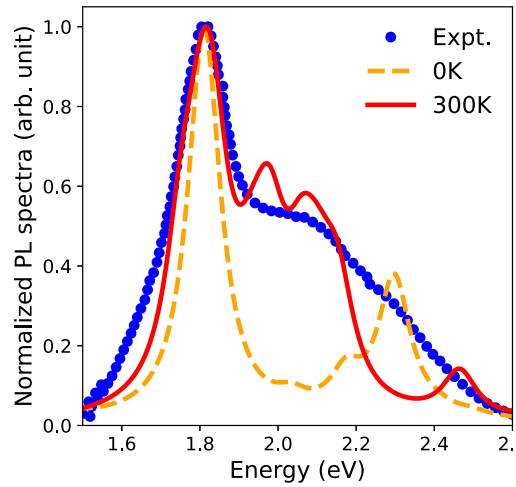

FIG. 4. The total photoluminescence spectra computed as averaging over the spectra computed for the single-defect geometries optimized at 0 K (orange dashed line) and sampled along the MD trajectories at 300 K (red line), and compared with the experimental spectrum (blue dots) taken from Ref. [20]. All the spectra are normalized, and the first peak in the computed spectra is aligned to the experimental one.

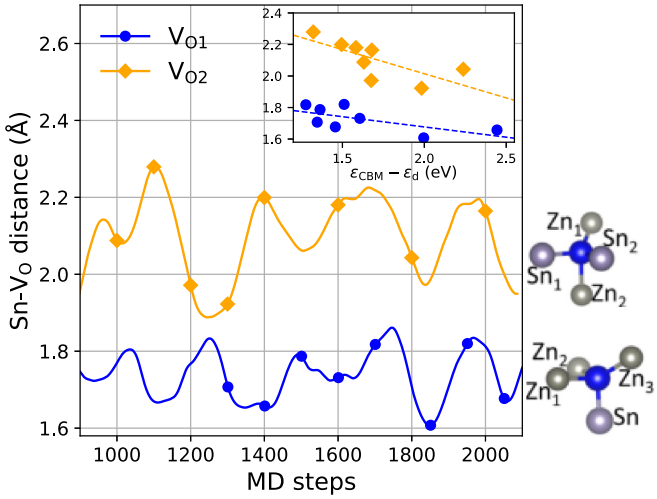

FIG. 5. Distance between the oxygen vacancy center and its nearest-neighbor Sn atoms computed for the V_{O1} (blue line) and V_{O2} (orange line) structures along their MD trajectory at 300 K. The ball-and-stick models represent the nearest-neighbor atoms to oxygen vacancies (blue balls) for the V_{O1} and V_{O2} structures; each of them is placed next to the corresponding MD trajectory. For the V_{O2} structure, the distance to the Sn_1 atom is considered (the distance to the Sn_2 atom is plotted in the Supplemental Material [42]). Eight MD samples chosen for computing the PL are denoted by the blue circles (V_{O1}) and orange diamonds (V_{O2}). The inset shows the relation between the above distance and the energy difference between the system's CBM and defect states computed for the eight samples. The linear fitting lines are also done for eye guiding.

using a leapfrog velocity Verlet algorithm to integrate the ionic equations of motion [53] as implemented in the CONQUEST code [54,55] with a time step of 1 fs. These structures are relaxed within 2 ps in the microcanonical (NVE) ensemble after 1 ps thermalization running within the NVT canonical ensemble using the stochastic velocity rescaling thermostat MD [56]. We only used this MD simulation on V_{O1} and V_{O2} structures that contribute to the interesting PL regime and computed the PL spectrum on their eight chosen samples along the NVE MD trajectory, as shown in Fig. 5. Details of each sample's PL spectrum are shown in Figs. 4 and 5 of the SM [42]. The electronic calculations show that while the band gap of the samples, $E_g = 2.92 \pm 0.04$ eV, is almost unchanged, the energy levels of oxygen vacancies are varied up to 1.2 eV upon the MD relaxation [42] (especially, those of V_{O2} vary more than those of V_{O1}). The latter induces changes in the PL spectra of both positions and intensities of the peaks for each configuration. The averaged spectrum of the 16 samples of V_O (300 K curve in Fig. 4) results in the computed PL spectrum in agreement with the experimental one, thus interpreting the discrepancy mentioned above. Details of each sample's PL spectrum are shown in Figs. 4 and 5 of the SM [42]. There is still a discrepancy between the experimental and the 300 K spectra between 2.3 and 2.5 eV. This energy window is larger than the the band-to-defect emission energy and thus requires another emission mechanism to interpret, which is however beyond the scope of this Letter.

To examine which factor affects the oxygen vacancy structures the most, we plot in Fig. 5 the distances between oxygen vacancy centers and their adjacent Sn atoms depending on the number of MD steps. We choose the Sn atom because the changes are more pronounced for the distance to Sn atoms than that to the Zn atom (see also Figs. 6–8 of the SM [42]). As found in Ref. [25], the strong hybridization between Sn atomic orbitals and oxygen vacancy states means that electronic properties and charge distribution around an oxygen vacancy are affected mainly by the adjacent Sn atom. Moreover, because of the multiple oxidation states, Sn atomic orbitals can be strongly bound to the defect states during the MD equilibration. Figure 5 shows that these distances oscillate strongly during the MD simulation, up to 12% more than their averaged distance in the pristine structure at zero temperature. More importantly, the inset of this figure shows the tendency of linear dependence between these distances and the defect energy states (with respect to the CBM), justifying the role of Sn atoms on oxygen vacancy energy levels. This role is also reflected via the stronger variation of the PL spectra of V_{O2} upon MD relaxation compared to the V_{O1}, where the V_{O2} is adjacent to two Sn atoms and the V_{O1} is adjacent to only one Sn atom.

In conclusion, we have investigated the PL spectrum of Zn_2SnO_4 using DFT calculations with the hybrid-PBE0 functional, which is a reliable and accurate tool for calculating this kind of spectrum. We calculated a theoretical spectrum that closely matches experiment at room temperature and predicted the spectrum at 0 K. In accordance with previous work, we provided further evidence of the origins of the bands between the far-red and green peaks in the experimental spectrum, which are mostly due to the oxygen vacancies in the systems. More importantly, we demonstrated that defect energy states, particularly for oxygen vacancy V_{O2}, are strongly influenced by thermal effects, fully explaining the difference in PL spectra at zero and room temperatures. In particular, the vibration of the metal atoms (Sn) around these oxygen vacancies due to thermal equilibration significantly affects the spectrum, justifying the impact of temperature on the PL spectrum.

ACKNOWLEDGMENTS

Our calculations in this Letter are performed using HPC Systems of Phenikaa University. The research is funded by Vietnam National Foundation for Science and Technology Development under Grant No. 103.02-2021.95.

[1] G. Fu, H. Chen, Z. Chen, J. Zhang, and H. Kohler, Humidity sensitive characteristics of Zn_2SnO_4-$LiZnVO_4$ thick films prepared by the sol-gel method, Sens. Actuators B **81**, 308 (2002).

[2] Y. Sato, J. Kiyohara, A. Hasegawa, T. Hattori, M. Ishida, N. Hamada, N. Oka, and Y. Shigesato, Study on inverse spinel zinc stannate, Zn_2SnO_4, as transparent conductive films deposited by rf magnetron sputtering, Thin Solid Films **518**, 1304 (2009).

[3] I. Arora and P. Kumar, Association of structure and modulated optoelectronic property in sb doped Zn_2SnO_4 nanostructured films for transparent electrodes, J. Alloys Compd. **845**, 156316 (2020).

[4] A. Rong, X. P. Gao, G. R. Li, T. Y. Yan, H. Y. Zhu, J. Q. Qu, and D. Y. Song, Hydrothermal synthesis of Zn_2SnO_4 as anode materials for Li-ion battery, J. Phys. Chem. B **110**, 14754 (2006).

[5] X. J. Zhu, L. M. Geng, F. Q. Zhang, Y. X. Liu, and L. B. Cheng, Synthesis and performance of Zn_2SnO_4 as anode materials for lithium ion batteries by hydrothermal method, J. Power Sources **189**, 828 (2009).

[6] C. Yan, J. Yang, Q. Xie, Z. Lu, B. Liu, C. Xie, S. Wu, Y. Zhang, and Y. Guan, Novel nanoarchitectured Zn_2SnO_4 anchored on porous carbon as high performance anodes for lithium ion batteries, Mater. Lett. **138**, 120 (2015).

[7] B. Tan, E. Toman, Y. Li, and Y. Wu, Zinc stannate (Zn_2SnO_4) dye-sensitized solar cells, J. Am. Chem. Soc. **129**, 4162 (2007).

[8] T. Lana-Villarreal, G. Boschloo, and A. Hagfeldt, Nanostructured zinc stannate as semiconductor working electrodes for dye-sensitized solar cells, J. Phys. Chem. C **111**, 5549 (2007).

[9] Y. Lin, S. Lin, M. Luo, and J. Liu, Enhanced visible light photocatalytic activity of Zn_2SnO_4 via sulfur anion-doping, Mater. Lett. **63**, 1169 (2009).

[10] M. A. Alpuche-Aviles and Y. Wu, Photoelectrochemical study of the band structure of Zn_2SnO_4 prepared by the hydrothermal method, J. Am. Chem. Soc. **131**, 3216 (2009).

[11] L. A. Joseph, J. E. Jeronsia, M. M. Jaculine, and S. J. Das, Investigations on structural and optical properties of hydrothermally synthesized Zn_2SnO_4 nanoparticles, Phys. Res. Int. **2016**, e1801795 (2016).

[12] J. X. Wang, S. S. Xie, H. J. Yuan, X. Q. Yan, D. F. Liu, Y. Gao, Z. P. Zhou, L. Song, L. F. Liu, X. W. Zhao, X. Y. Dou, W. Y. Zhou, and G. Wang, Synthesis, structure, and photoluminescence of Zn_2SnO_4 single-crystal nanobelts and nanorings, Solid State Commun. **131**, 435 (2004).

[13] L. Wang, X. Zhang, X. Liao, and W. Yang, A simple method to synthesize single-crystalline Zn_2SnO_4 (ZTO) nanowires and their photoluminescence properties, Nanotechnology **16**, 2928 (2005).

[14] S. Yang and J. Zhang, Orange photoluminescence emission and multi-photon Raman scattering from microscale Zn_2SnO_4 tetrapods, Chem. Phys. Lett. **712**, 40 (2018).

[15] Q. R. Hu, P. Jiang, H. Xu, Y. Zhang, S. L. Wang, X. Jia, and W. H. Tang, Synthesis and photoluminescence of Zn_2SnO_4 nanowires, J. Alloys Compd. **484**, 25 (2009).

[16] L. T. T. Vien, N. Tu, D. X. Viet, D. D. Anh, D. H. Nguyen, and P. T. Huy, Mn^{2+}-doped Zn_2SnO_4 green phosphor for WLED applications, J. Lumin. **227**, 117522 (2020).

[17] X. Huang, Red phosphor converts white LEDs, Nat. Photonics **8**, 748 (2014).

[18] M. T. Tran, D. Q. Trung, N. Tu, D. D. Anh, L. T. H. Thu, N. V. Du, N. V. Quang, N. T. Huyen, N. D. T. Kien, D. X. Viet, N. D. Hung, and P. T. Huy, Single-phase far-red-emitting $ZnAl_2O_4$: Cr^{3+} phosphor for application in plant growth LEDs, J. Alloys Compd. **884**, 161077 (2021).

[19] X. Fu, X. Wang, J. Long, Z. Ding, T. Yan, G. Zhang, Z. Zhang, H. Lin, and X. Fu, Hydrothermal synthesis, characterization, and photocatalytic properties of Zn_2SnO_4, J. Solid State Chem. **182**, 517 (2009).

[20] L. T. T. Vien, N. Tu, M. T. Tran, N. Van Du, D. H. Nguyen, D. X. Viet, N. V. Quang, D. Q. Trung, and P. T. Huy, A new far-red emission from Zn_2SnO_4 powder synthesized by modified solid state reaction method, Opt. Mater. (Amsterdam) **100**, 109670 (2020).

[21] S. Jeedigunta, M. K. Singh, A. Kumar, and M. Shamsuzzoha, Optical properties of zigzag twinned geometry of Zn_2SnO_4 nanowires, J. Nanosci. Nanotechnol. **7**, 486 (2007).

[22] B. R. Yakami, U. Poudyal, S. R. Nandyala, G. Rimal, J. K. Cooper, X. Zhang, J. Wang, W. Wang, and J. M. Pikal, Steady state and time resolved optical characterization studies of Zn_2SnO_4 nanowires for solar cell applications, J. Appl. Phys. **120**, 163101 (2016).

[23] J.-W. Zhao, L.-R. Qin, and L.-D. Zhang, Single-crystalline Zn_2SnO_4 hexangular microprisms: Fabrication, characterization and optical properties, Solid State Commun. **141**, 663 (2007).

[24] A. Annamalai, D. Carvalho, K. C. Wilson, and M.-J. Lee, Properties of hydrothermally synthesized Zn_2SnO_4 nanoparticles using Na_2CO_3 as a novel mineralizer, Mater. Charact. **61**, 873 (2010).

[25] J. Lee, Y. Kang, C. S. Hwang, S. Han, S.-C. Lee, and J.-H. Choi, Effect of oxygen vacancy on the structural and electronic characteristics of crystalline Zn_2SnO_4, J. Mater. Chem. C **2**, 8381 (2014).

[26] D. L. Young, H. Moutinho, Y. Yan, and T. J. Coutts, Growth and characterization of radio frequency magnetron sputter-deposited zinc stannate, Zn_2SnO_4, thin films, J. Appl. Phys. **92**, 310 (2002).

[27] D. L. Young, D. L. Williamson, and T. J. Coutts, Structural characterization of zinc stannate thin films, J. Appl. Phys. **91**, 1464 (2002).

[28] R. Guo, H. Li, and H. Liu, Phase investigation and crystal structure analysis of zinc stannate (Zn_2SnO_4), Phys. Lett. A **384**, 126205 (2020).

[29] G. B. Palmer and K. R. Poeppelmeier, Phase relations, transparency and conductivity in Ga_2O_3-SnO_2-ZnO, Solid State Sci. **4**, 317 (2002).

[30] S. P. Harvey, K. R. Poeppelmeier, and T. O. Mason, Subsolidus phase relationships in the ZnO-In_2O_3-SnO_2 system, J. Am. Ceram. Soc. **91**, 3683 (2008).

[31] J. Lee, S.-C. Lee, C. S. Hwang, and J.-H. Choi, Thermodynamic stability of various phases of zinc tin oxides from *ab initio* calculations, J. Mater. Chem. C **1**, 6364 (2013).

[32] A. Seko, F. Oba, and I. Tanaka, Classification of spinel structures based on first-principles cluster expansion analysis, Phys. Rev. B **81**, 054114 (2010).

[33] L. Bao, J. Zang, G. Wang, and X. Li, Atomic-scale imaging of cation ordering in inverse spinel Zn_2SnO_4 nanowires, Nano Lett. **14**, 6505 (2014).

[34] L. Gracia, A. Beltrán, and J. Andrés, A theoretical study on the pressure-induced phase transitions in the inverse spinel structure Zn_2SnO_4, J. Phys. Chem. C **115**, 7740 (2011).

[35] P. P. Das, P. S. Devi, D. A. Blom, T. Vogt, and Y. Lee, High-pressure phase transitions of morphologically distinct Zn_2SnO_4 nanostructures, ACS Omega **4**, 10539 (2019).

[36] A. Jain, S. P. Ong, G. Hautier, W. Chen, W. D. Richards, S. Dacek, S. Cholia, D. Gunter, D. Skinner, G. Ceder, and K. A. Persson, Commentary: The Materials Project: A materials genome approach to accelerating materials innovation, APL Mater. **1**, 011002 (2013).

[37] M. Parrinello and A. Rahman, Polymorphic transitions in single crystals: A new molecular dynamics method, J. Appl. Phys. **52**, 7182 (1981).

[38] P. Giannozzi, S. Baroni, N. Bonini, M. Calandra, R. Car, C. Cavazzoni, D. Ceresoli, G. L. Chiarotti, M. Cococcioni, I. Dabo, A. D. Corso, S. de Gironcoli, S. Fabris, G. Fratesi, R. Gebauer, U. Gerstmann, C. Gougoussis, A. Kokalj, M. Lazzeri, L. Martin-Samos, N. Marzari, F. Mauri, R. Mazzarello, S. Paolini, A. Pasquarello, L. Paulatto, C. Sbraccia, S. Scandolo, G. Sclauzero, A. P. Seitsonen, A. Smogunov, P. Umari, and R. M. Wentzcovitch, QUANTUM ESPRESSO: A modular and open-source software project for quantum simulations of materials, J. Phys.: Condens. Matter **21**, 395502 (2009).

[39] P. Giannozzi, O. Andreussi, T. Brumme, O. Bunau, M. B. Nardelli, M. Calandra, R. Car, C. Cavazzoni, D. Ceresoli, M. Cococcioni, N. Colonna, I. Carnimeo, A. D. Corso, S. de Gironcoli, P. Delugas, R. A. DiStasio, A. Ferretti, A. Floris, G. Fratesi, G. Fugallo, R. Gebauer, U. Gerstmann, F. Giustino, T. Gorni, J. Jia, M. Kawamura, H.-Y. Ko, A. Kokalj, E. Küçükbenli, M. Lazzeri, M. Marsili, N. Marzari, F. Mauri, N. L. Nguyen, H.-V. Nguyen, A. Otero-de-la-Roza, L. Paulatto, S. Poncé, D. Rocca, R. Sabatini, B. Santra, M. Schlipf, A. P. Seitsonen, A. Smogunov, I. Timrov, T. Thonhauser, P. Umari, N. Vast, X. Wu, and S. Baroni, Advanced capabilities for materials modelling with Quantum ESPRESSO, J. Phys.: Condens. Matter **29**, 465901 (2017).

[40] R. Fletcher, Newton-like methods, in *Practical Methods of Optimization* (Wiley, New York, 2000), Chap. 3, pp. 44–79.

[41] M. Schlipf and F. Gygi, Optimization algorithm for the generation of ONCV pseudopotentials, Comput. Phys. Commun. **196**, 36 (2015).

[42] See Supplemental Material at http://link.aps.org/supplemental/10.1103/PhysRevB.107.L060102 for details of the atomic coordinates of the defect structures, the defect state energy induced by the 12 defect structures and their density isosurface plots, the individual PL from 12 defect structures at 0 K and 16 V_O structures sampled along the NVE-MD trajectory at 300 K, and the variation of distances between the oxygen vacancy centers and their nearest-neighbor Sn and Zn atoms upon MD simulation.

[43] H. B. Bebb and E. W. Williams, Photoluminescence I: Theory, in *Semiconductors and Semimetals*, edited by R. K. Willardson and A. C. Beer (Elsevier, Amsterdam, 1972), Vol. 8, Chap. 4, pp. 181–320.

[44] P. Y. Yu and M. Cardona, *Fundamentals of Semiconductors*, Graduate Texts in Physics (Springer-Verlag, Berlin, 2010).

[45] J. P. Perdew, K. Burke, and M. Ernzerhof, Generalized Gradient Approximation Made Simple, Phys. Rev. Lett. **77**, 3865 (1996).

[46] J. P. Perdew, M. Ernzerhof, and K. Burke, Rationale for mixing exact exchange with density functional approximations, J. Chem. Phys. **105**, 9982 (1996).

[47] Y. Zhao, L. Hu, H. Liu, M. Liao, X. Fang, and L. Wu, Band gap tunable Zn_2SnO_4 nanocubes through thermal effect and their outstanding ultraviolet light photoresponse, Sci. Rep. **4**, 6847 (2014).

[48] J. P. Perdew and A. Zunger, Self-interaction correction to density-functional approximations for many-electron systems, Phys. Rev. B **23**, 5048 (1981).

[49] N. L. Nguyen, N. Colonna, A. Ferretti, and N. Marzari, Koopmans-Compliant Spectral Functionals for Extended Systems, Phys. Rev. X **8**, 021051 (2018).

[50] G. Onida, L. Reining, and A. Rubio, Electronic excitations: Density-functional versus many-body Green's-function approaches, Rev. Mod. Phys. **74**, 601 (2002).

[51] Y. Wang, J. Piao, G. Xing, Y. Lu, Z. Ao, N. Bao, J. Ding, S. Li, and J. Yi, Zn vacancy induced ferromagnetism in K doped ZnO, J. Mater. Chem. C **3**, 11953 (2015).

[52] D. Kim, J.-h. Yang, and J. Hong, Ferromagnetism induced by Zn vacancy defect and lattice distortion in ZnO, J. Appl. Phys. **106**, 013908 (2009).

[53] M. P. Allen and D. J. Tildesley, *Computer Simulation of Liquids* (Clarendon, Oxford, 1989).

[54] T. Miyazaki, D. R. Bowler, R. Choudhury, and M. J. Gillan, Atomic force algorithms in density functional theory electronic-structure techniques based on local orbitals, J. Chem. Phys. **121**, 6186 (2004).

[55] D. R. Bowler, R. Choudhury, M. J. Gillan, and T. Miyazaki, Recent progress with large-scale ab initio calculations: The CONQUEST code, Phys. Status Solidi B **243**, 989 (2006).

[56] G. Bussi, D. Donadio, and M. Parrinello, Canonical sampling through velocity rescaling, J. Chem. Phys. **126**, 014101 (2007).